Synthesis of two-dimensional N-terminated molybdenum carbides by alloying strategy in molten salt

Weiyan Jiang[a,b,c],‡ ZihanGao[a,b,c],‡ Miao Shen[a,b,c,*], Rui Tang[a,b,c], Jing Zhou[d,*], Chuanqiang Wu[e], Linjuan Zhang[a,b,c], Jian-Qiang Wang[a,b,c,*]

[a] Shanghai Institute of Applied Physics, Chinese Academy of Sciences, Shanghai 201800, P.R. China

[b] University of Chinese Academy of Sciences, Beijing 100049, P.R. China

[c] Key Laboratory of Interfacial Physics and Technology, Chinese Academy of Sciences, Shanghai 201800, P.R. China

[d] Zhejiang Institute of Photoelectronics & Zhejiang Institute for Advanced Light Source, Zhejiang Normal University, Jinhua, Zhejiang 321004, P. R. China

[e] Information Materials and Intelligent Sensing Laboratory of Anhui Province, Key Laboratory of Structure and Functional Regulation of Hybrid Materials of Ministry of Education; Institutes of Physical Science and Information Technology, Anhui University, Hefei 230601, P.R. China

* Corresponding Author

E-mail: shenmiao@sinap.ac.cn (M. Shen), zhoujing5457@zjnu.edu.cn (J. Zhou), wangjianqiang@sinap.ac.cn(J.-Q. Wang)

‡These authors contributed equally to this work.

Fig. S1 The pressed pellet sample (the diameter of 12 mm) of Ni/Li_3N/Mo_2Ga_2C with KCl-LiCl molten salts.

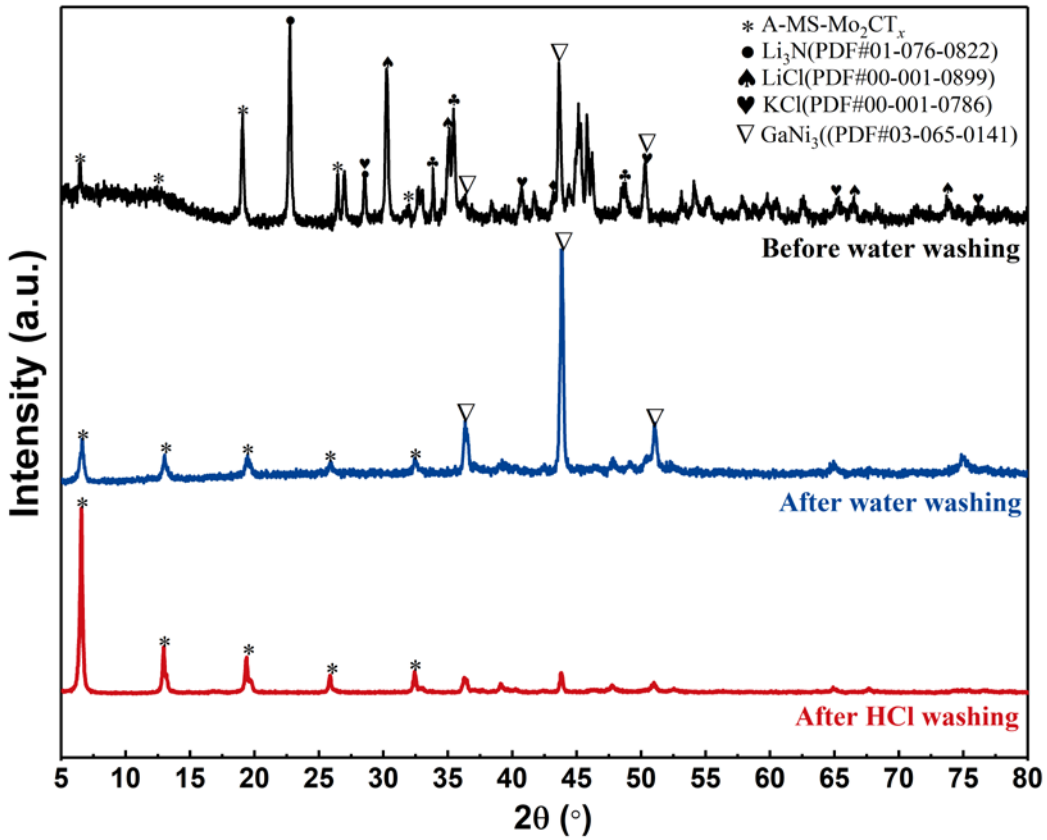

Fig. S2 XRD of the products for Ni-Li_3N-Mo_2Ga_2C-(KCl-LiCl) after reaction at 700℃ and the products washed by deionized water and HCl.

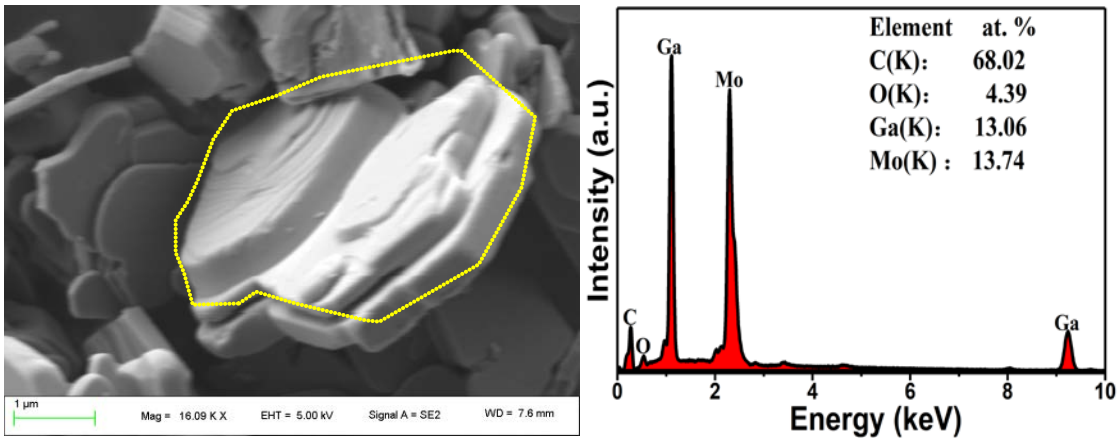

Fig. S3 SEM mages and EDS data of Mo_2Ga_2C materials.

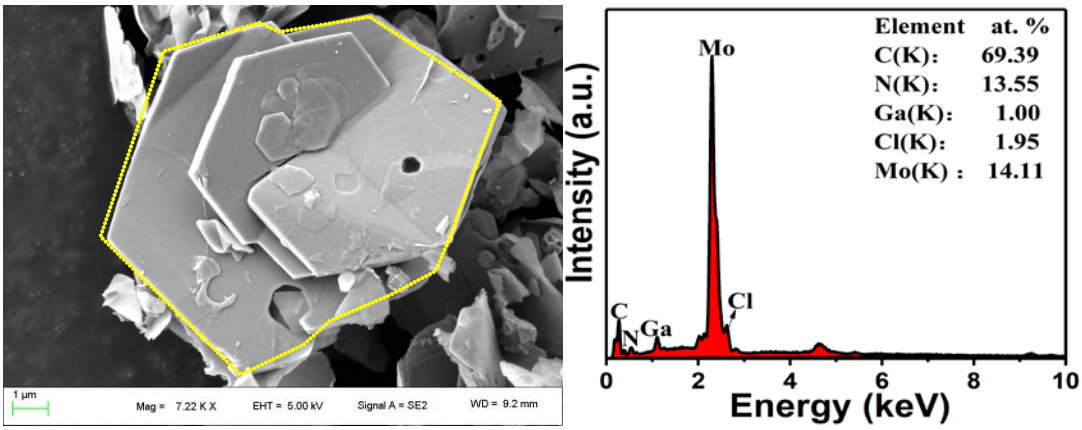

Fig. S4 SEM mages and EDS of A-MS-Mo_2CT_x.

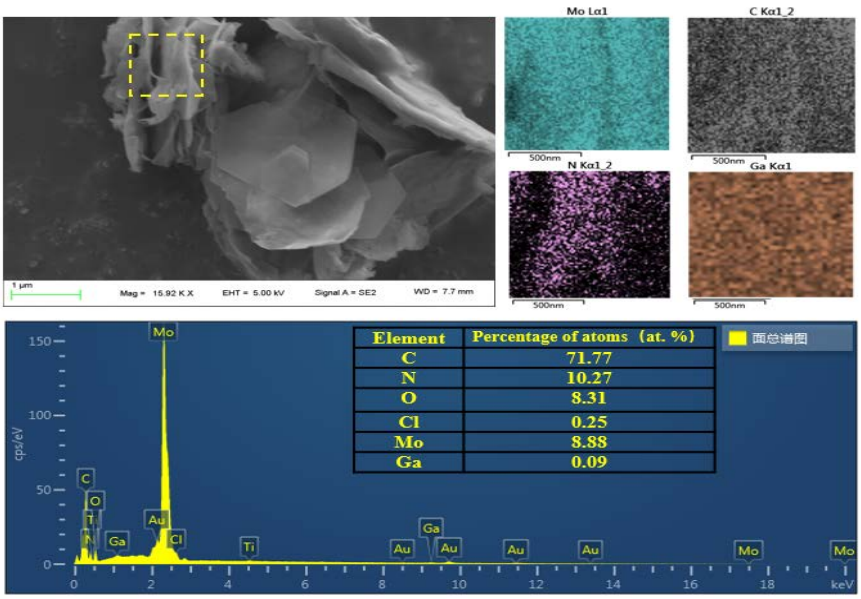

Fig. S5 SEM and EDS of Mo_2CT_x sample etched at 48h.

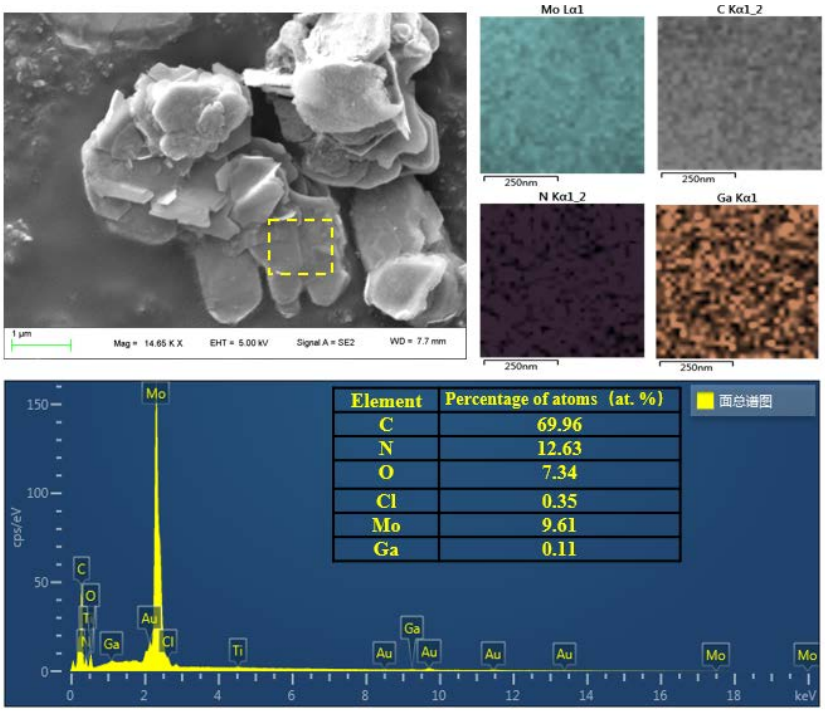

Fig. S6 SEM and EDS of Mo_2CT_x sample etched at 800 ℃.

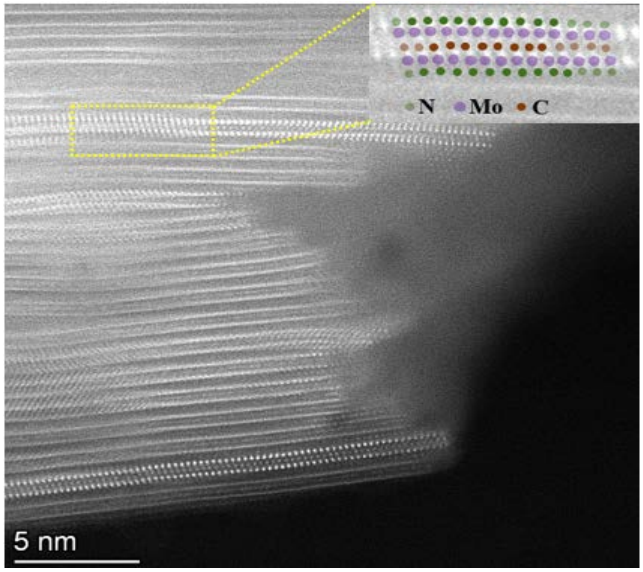

Fig. S7 HAADF of A-MS-Mo_2CT_x nanoflakes.

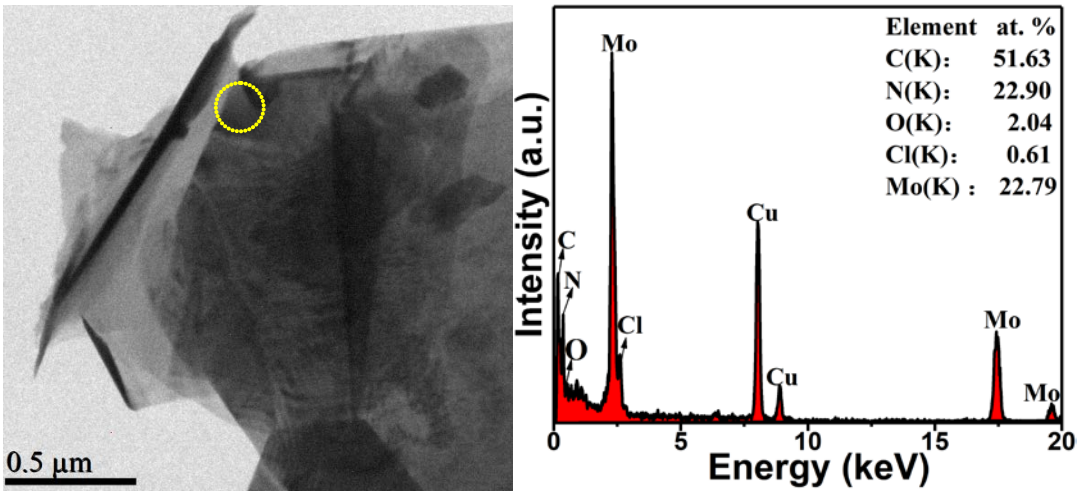

Fig. S8 Atomic percentage distribution of elements and EDX of A-MS-Mo_2CT_x from TEM-EDX.

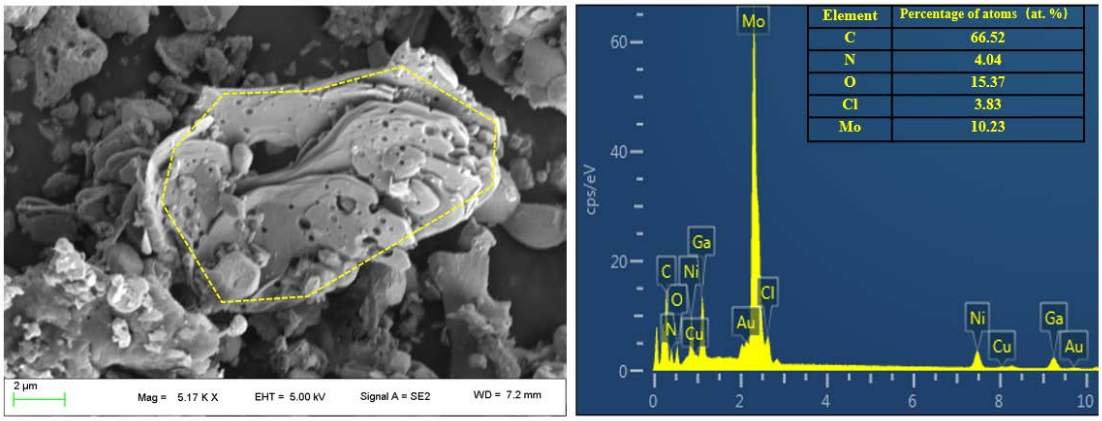

Fig.S9 SEM images and EDS of Mo_2CT_x produced at 1:0.33 mass ratio of Mo_2Ga_2C to Li_3N.

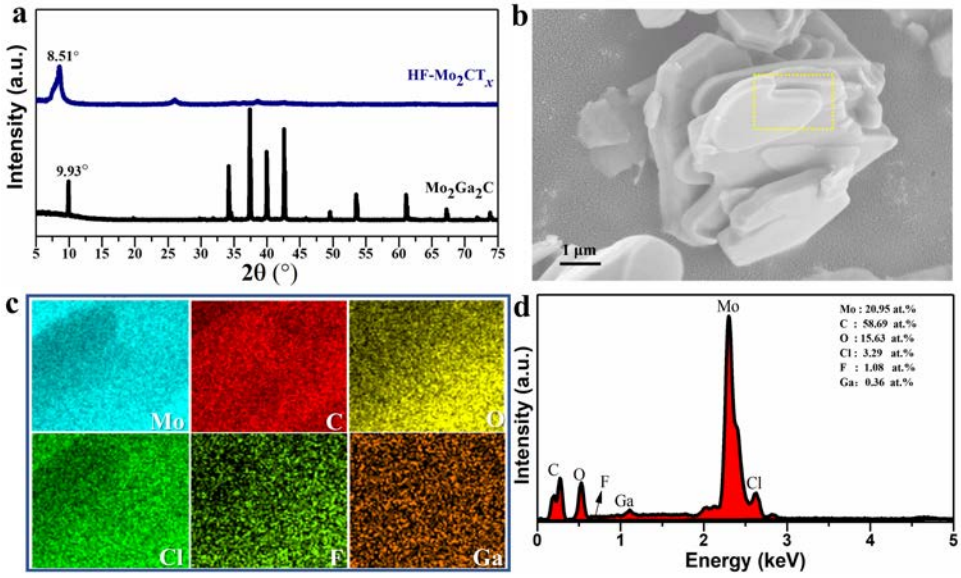

Fig. S10 (a) XRD, (b) SEM, (c) EDS and (d) The corresponding atomic percentage distribution of elements of HF-Mo_2CT_x samples by HF etching.

The characteristic peak of (002) for HF-Mo_2CT_x samples shifted lower angle (8.51°) from 9.93° of Mo_2Ga_2C, which indicates the Mo_2Ga_2C was effectively etched.[1, 2] SEM-EDS shows that the elements of O, Cl and Fare evenly distributed on the surface of HF-Mo_2CT_x. Among them, the relative content of O termination reached 15.63 at. %.

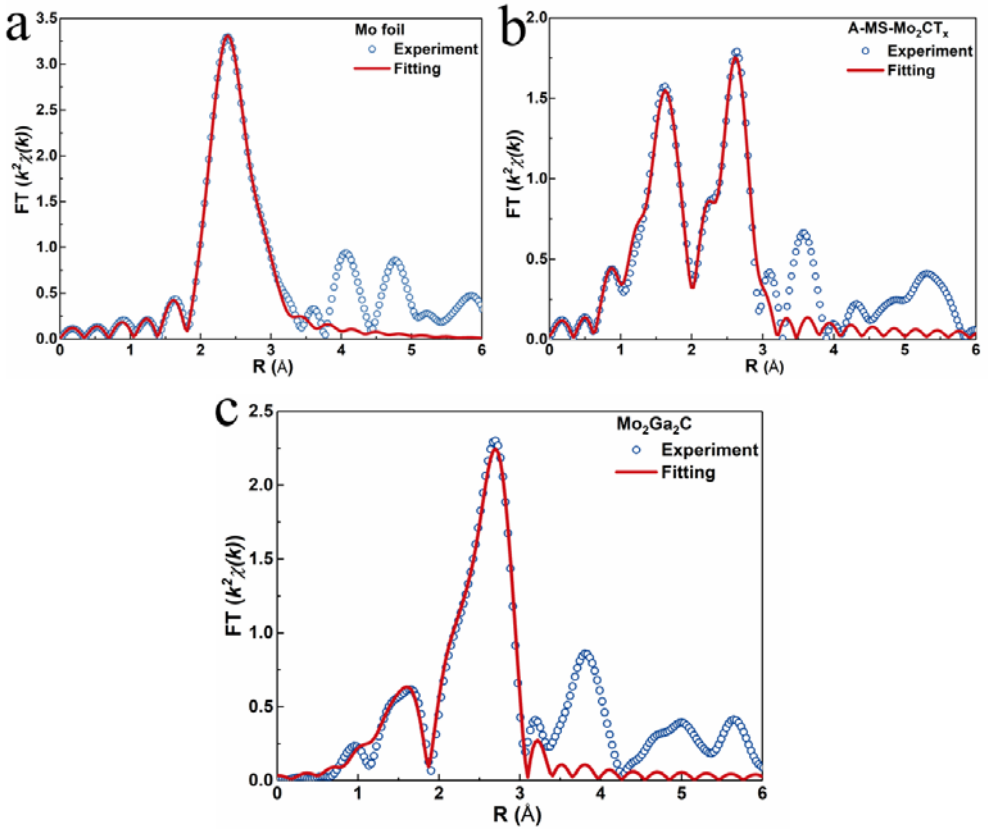

Fig. S11 EXAFS fittings of (a) Mo foil, (b)A-MS-Mo_2CT_x and(c)Mo_2Ga_2C.

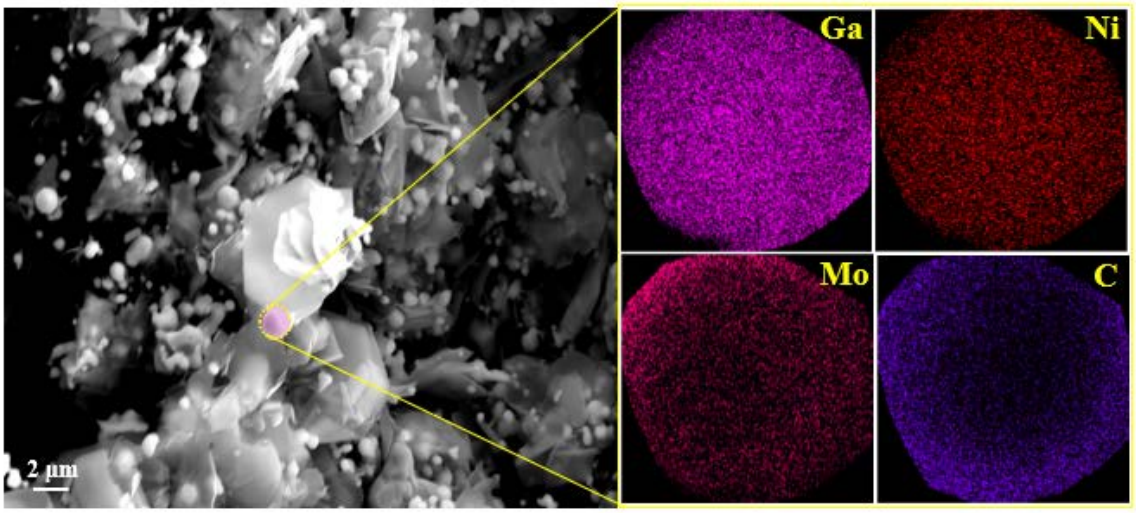

Fig. S12 The surface morphology and elemental distribution of by-products $GaNi_3$ alloy from SEM-EDX.

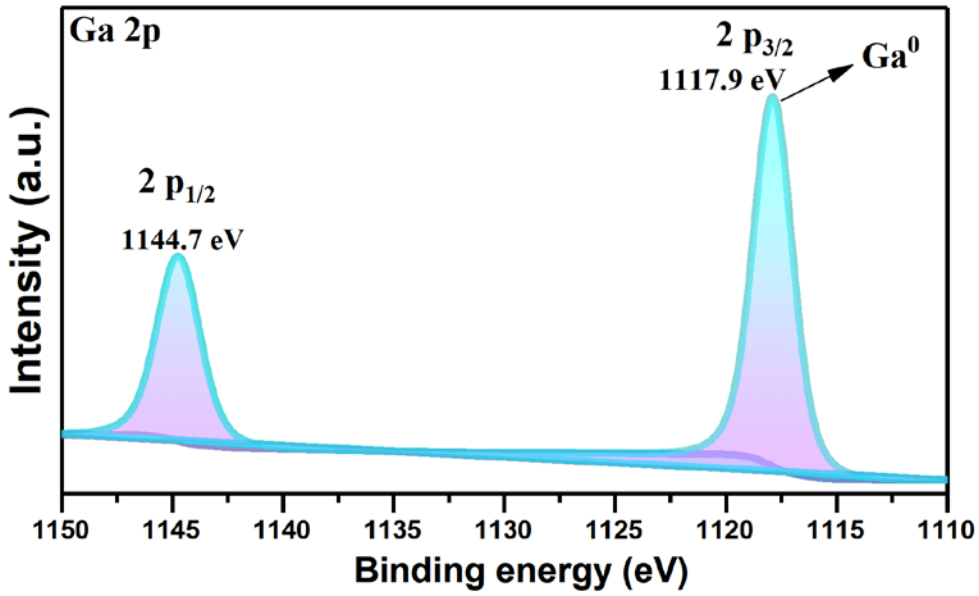

Fig. S13 Ga 2p of Mo_2Ga_2C from XPS.

The peak located at 1117.9 eV was corresponded to Ga^0, which is consistent with the analysis in the literature.[3, 4]

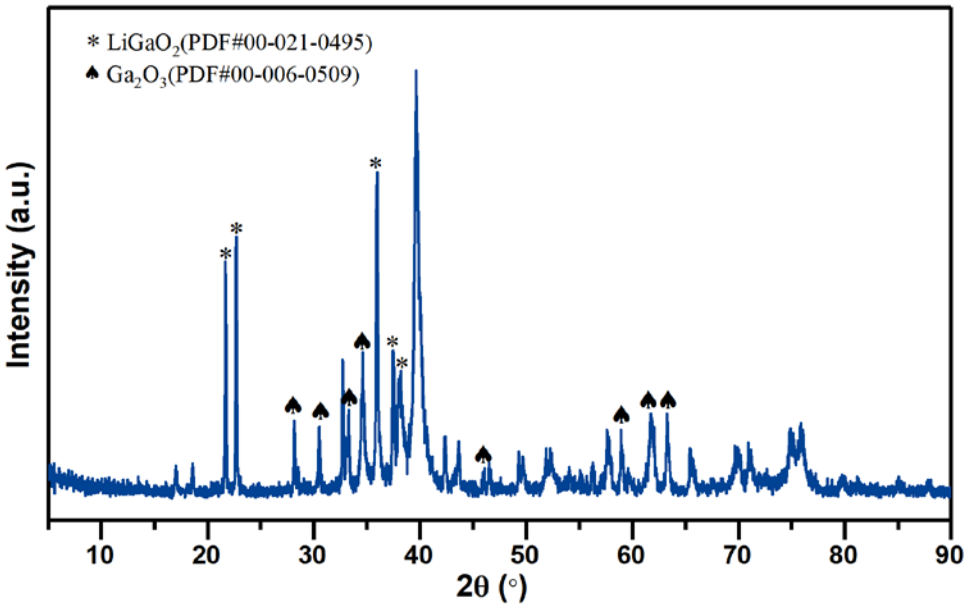

Fig. S14 Products of the reaction between LiOH and Mo_2Ga_2C.

Considering that Li_3N is easily hydrolyzed to LiOH ($Li_3N+3H_2O = 3LiOH + NH_3$), and LiOH is oxidizing, it will oxidize and etch Ga in Mo_2Ga_2C.

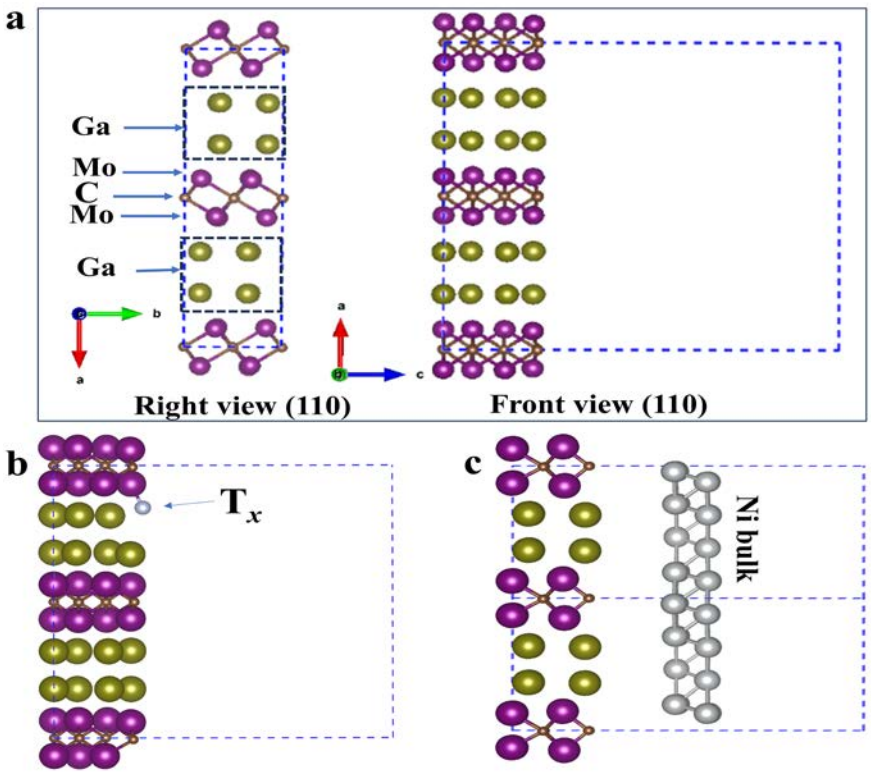

Fig. S15 The simulation models of supercell structure for adsorption calculation and searching TS. (a) the [110] surfaces of Mo_2Ga_2C supercells, (b) the searching TS model on the [110] surface, (c) the adsorption calculation model on the [110] surface.

Considering that the removal of Ga atoms along the crystal surface in the [110] direction, and the formation of functional groups on the Mo surface in [110] directionduring alloying processing.

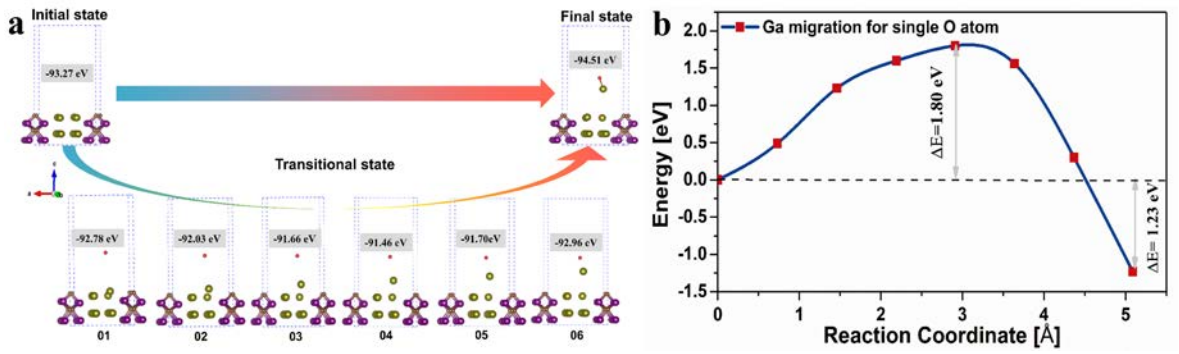

Fig. S16 Transition state calculations of the process of migration of interlayer Ga atoms out of Mo_2Ga_2C layer and interaction with single O atom.

In view of the initial formation of Ga_2O_3, we also established the model of Ga atoms migration from Mo_2Ga_2C to form Ga-O bond with O atoms. The calculation results show that the reaction energy of Ga atom to form Ga-O bondin Ga_2O_3 with O atom through migration is 1.8 eV. Therefore, it is reasonable to select "Mo_2Ga_2C + Ga_2O_3 and Ga defects" as transition states to calculate the energy barrier of the oxidation path.

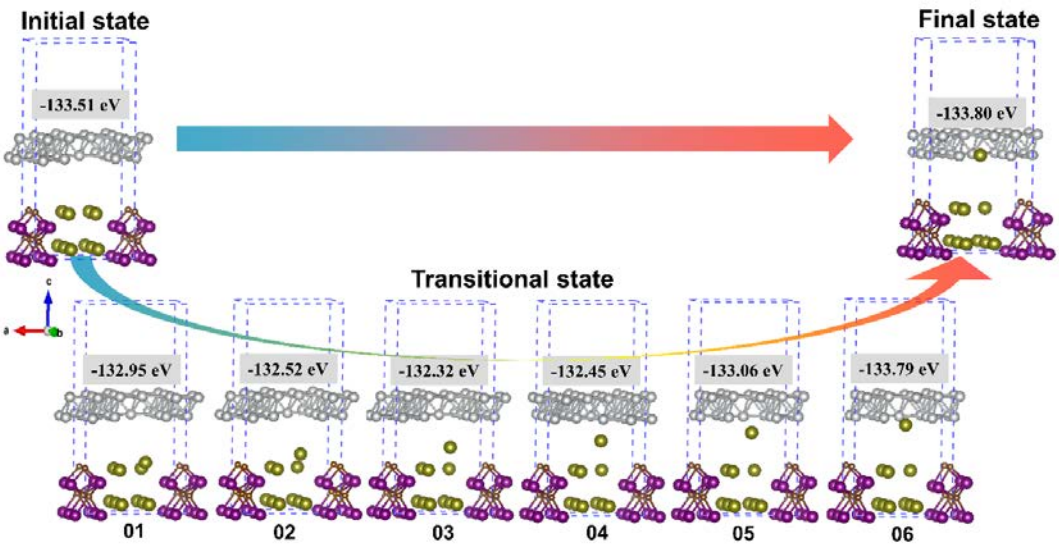

Fig. S17 Transition state models of Ga alloying-etching process for (110) plane of heterostructure $Mo_8Ga_8C_4$ and Ni_7*.

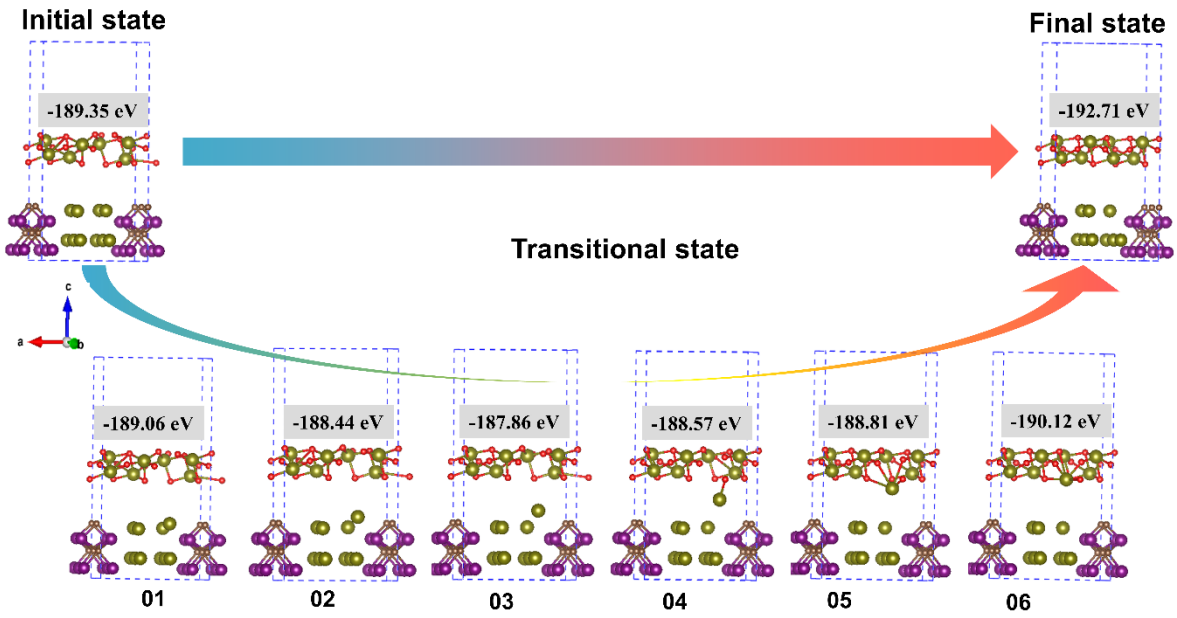

Fig. S18 Transition state models of Ga redox-etching process for (110) plane of heterostructure $Mo_8Ga_8C_4$ and Ga_3O_6*.

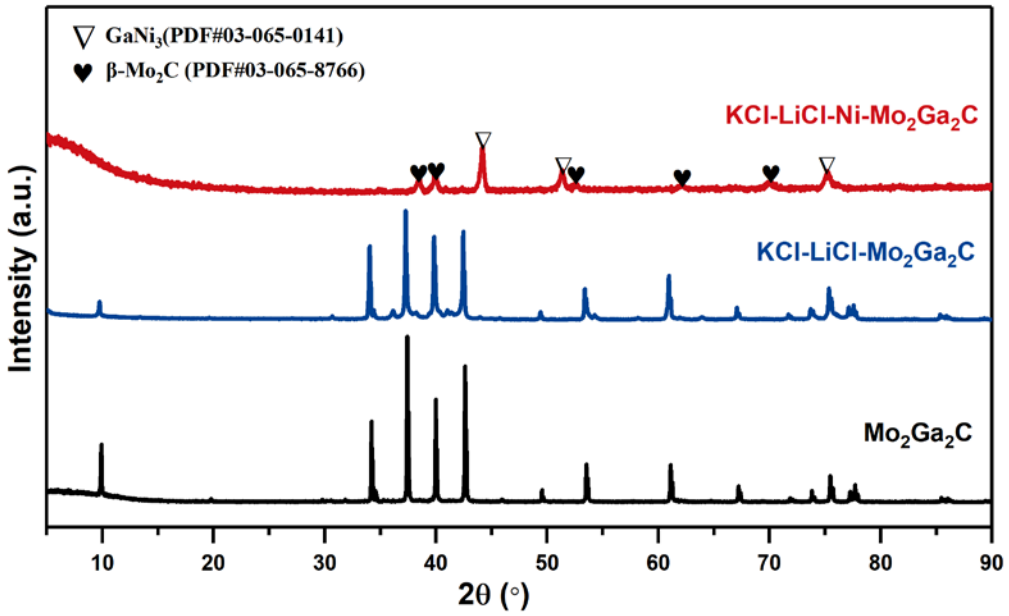

Fig. S19 XRD of product components of KCl-LiCl-Ni-Mo_2Ga_2C without Li_3N, KCl-LiCl-$Mo_2Ga_2C$and Mo_2Ga_2C at 700℃ for 24 h.

For KCl-LiCl-Ni-Mo_2Ga_2C system without Li_3N, the products are $GaNi_3$ and β-Mo_2C. However, in the system of KCl-LiCl-Mo_2Ga_2C, the raw material Mo_2Ga_2C did not change significantly.

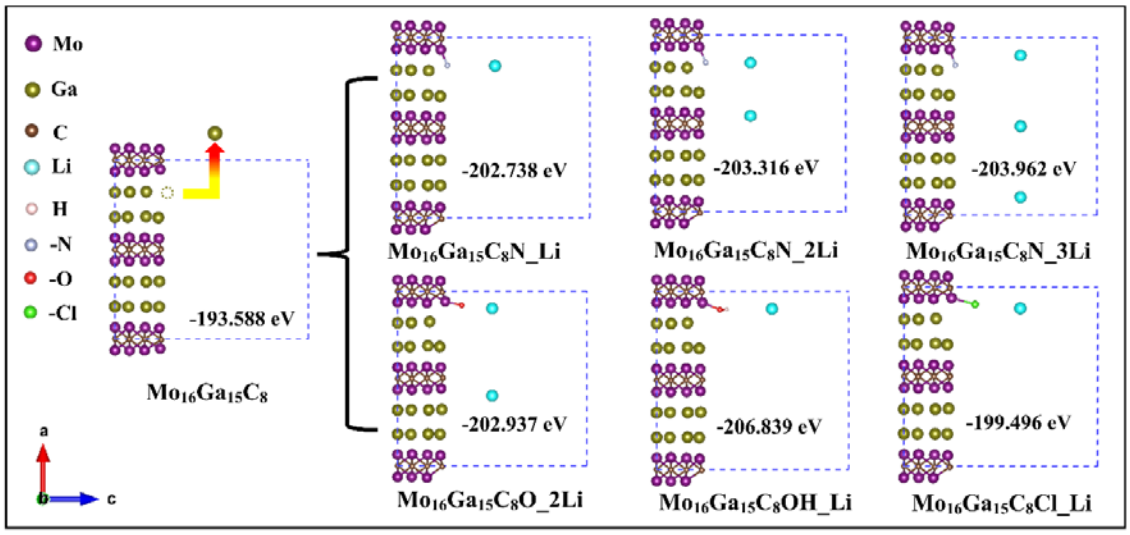

Fig. S20 The surface adsorption model and adsorption energy of single termination.

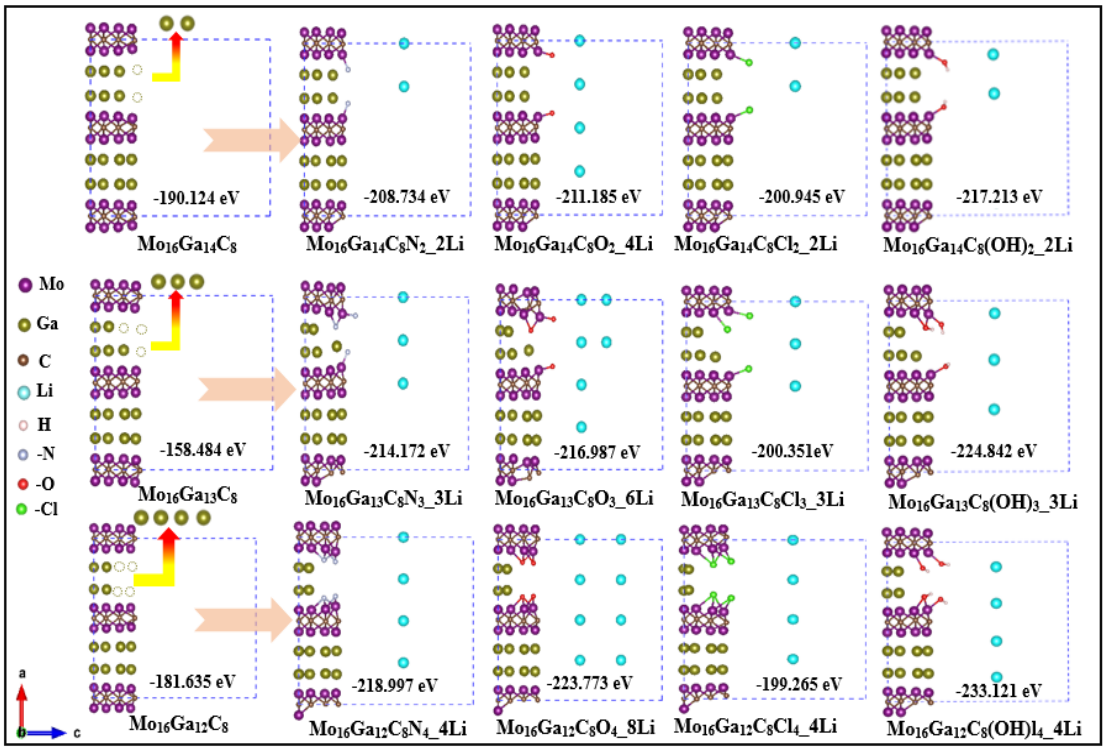

Fig. S21 The surface adsorption model and adsorption energy of different terminations.

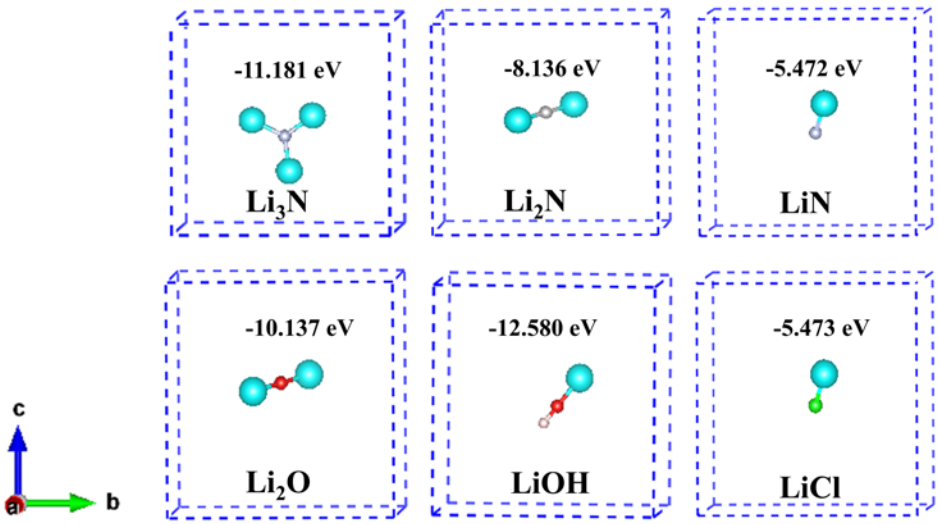

Fig. S22 Calculation of different singlefunctional groups in a vacuum box.

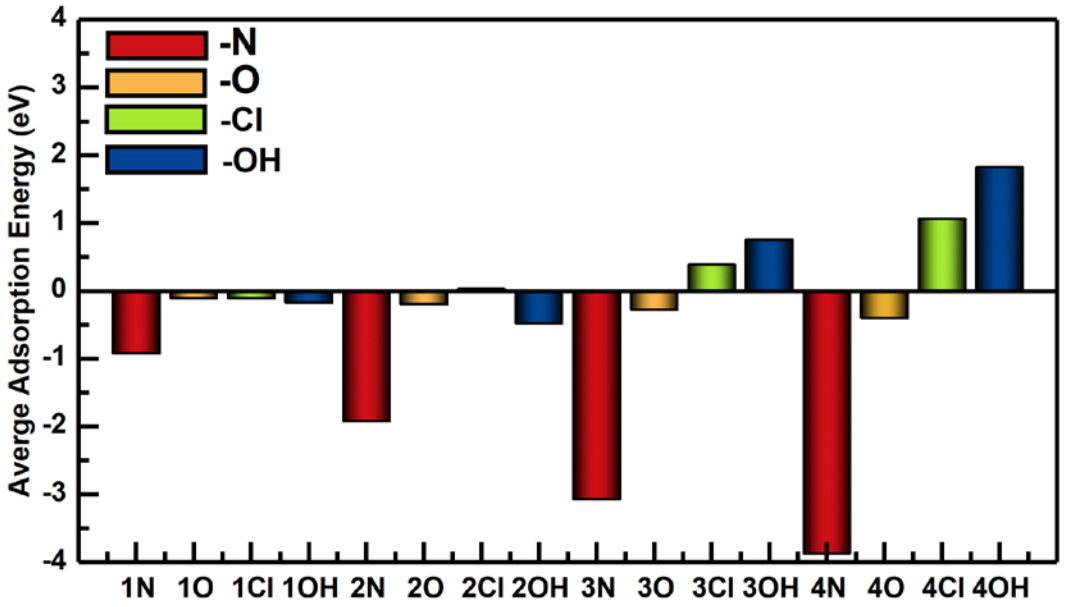

Fig. S23 The relationship between averagesurface adsorption energy and the number of adsorbed functional groups from LiN,Li_2O, LiCl and LiOH, respectively.

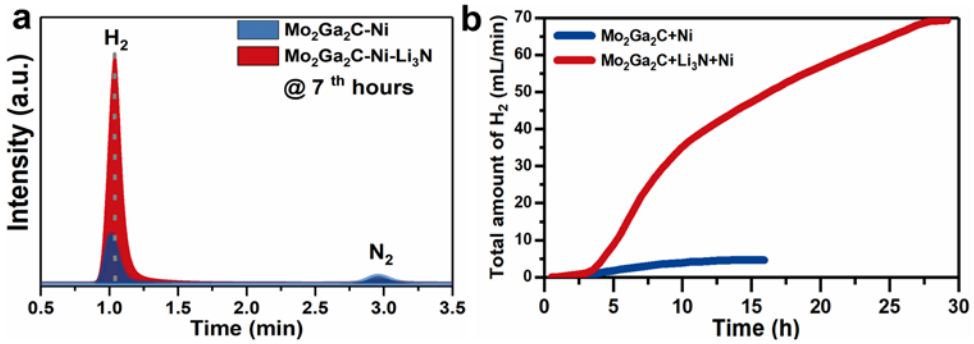

Fig. S24 (a) The hydrogen production rate and (b) total hydrogen productionduring reaction of Mo_2Ga_2C-Ni-Li_3N and Mo_2Ga_2C-Ni system in KCl-LiCl molten salt.

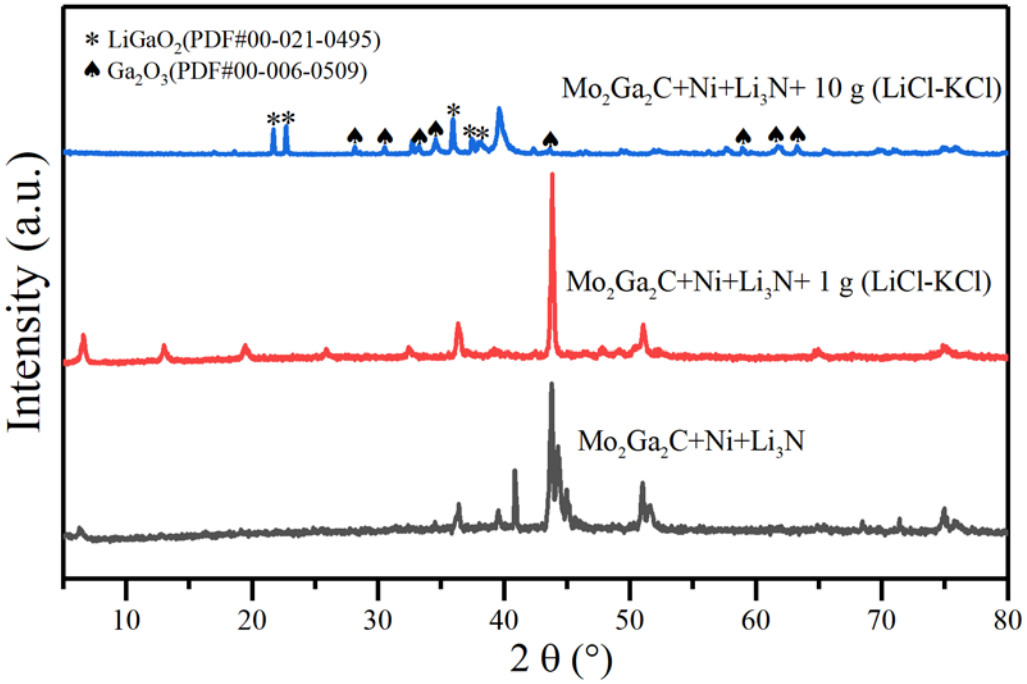

Fig. S25 XRD of products of Ni-Li_3N-Mo_2Ga_2C with and without KCl-LiCl liquid medium at 700°C for 24 h.

When the contents of Li_3N, Mo_2Ga_2C and iron ternary elements remained unchanged, and the LiCl-KCl eutectic salt increased from 1g to 10g, Mo_2CT_x products could not be obtained. This is probably because LiCl-KCl molten salt has a strong hygrometric property.With the increase of the mass of LiCl-KCl, the content of water adsorbed by LiCl-KCl will increase, and the amount of Li_3N converted to LiOH by reaction with water will increase. A large amount of LiOH will not only oxidize Ga to produce Ga_2O_3, but also oxidize Mo_2C, so no Mo_2CT_xproduct can be obtained.Without KCl-LiCl molten salt, the conversion rate of Mo_2Ga_2C to Mo_2CT_x products is considerably reduced. The results indicate that an optimal amount of LiCl-KCl is crucial for facilitating rapid migration, thereby enhancing the dissolution of reactants and diffusion rate of ions.

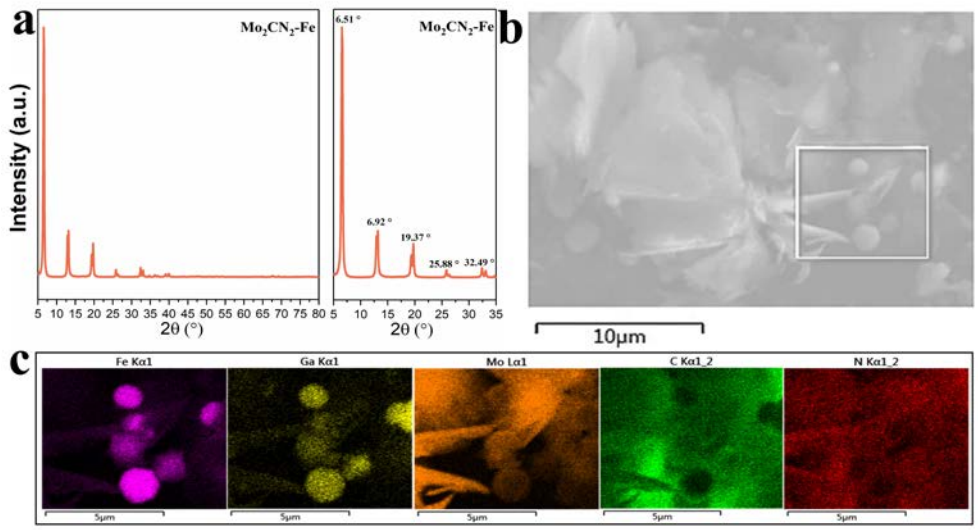

Fig. S26 The etching product of Mo_2Ga_2C in Fe-Li_3N-KCl-LiCl molten salts. (a) XRD of samples after HCl washing, (b) SEM and (c) EDS of the corresponding initial product samples.

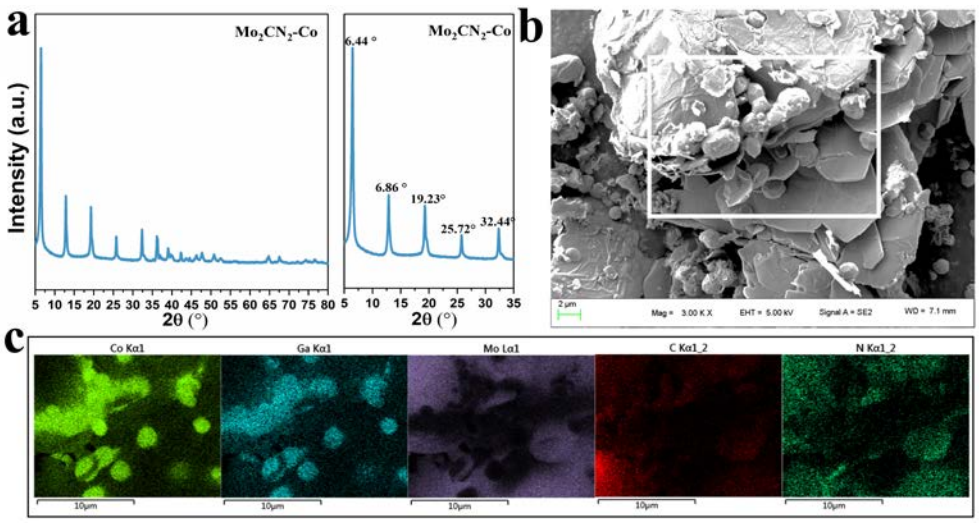

Fig. S27 The etching product of Mo_2Ga_2C in Co-Li_3N-KCl-LiCl molten salt. (a) XRD of samples after HCl washing, (b) SEM and (c) EDS of the corresponding initial product samples.

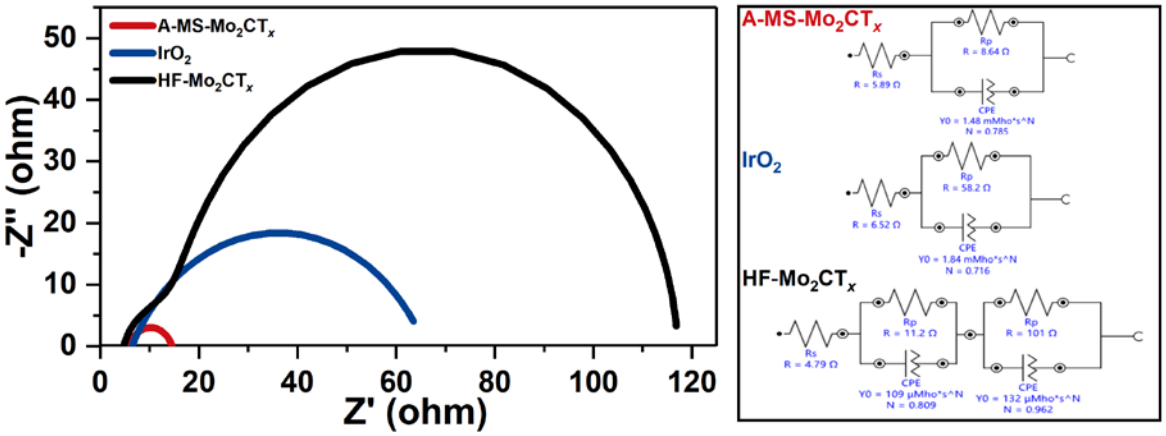

Fig. S28 EIS and equivalent simulation circuits of A-MS-Mo_2CT_x, IrO_2 and HF-Mo_2CT_x, respectively.

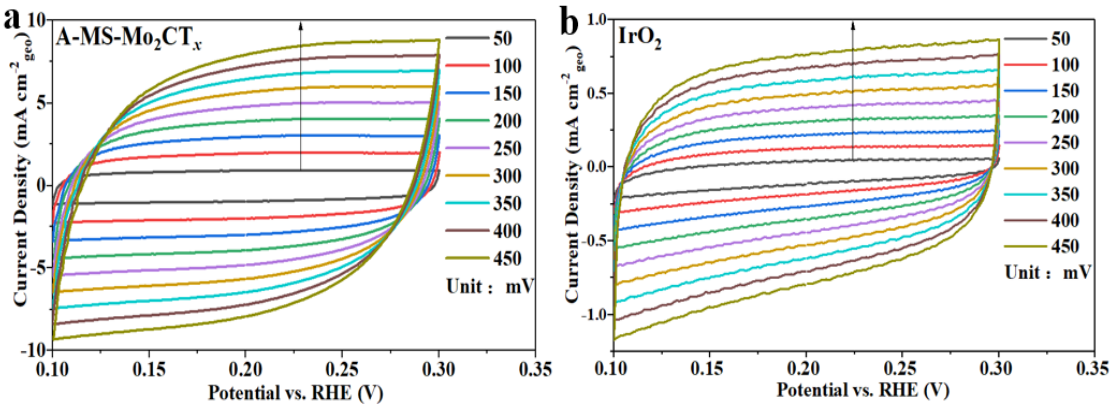

Fig. S29 Electrochemical capacitance measurements for (**a**) A-MS-$Mo_2CT_x$and (**b**) IrO_2 by using cyclic voltammetry at increasing scan rates (50,100, 150, 200, 250, 300, 350, 400 and 450 mV s^{-1}).

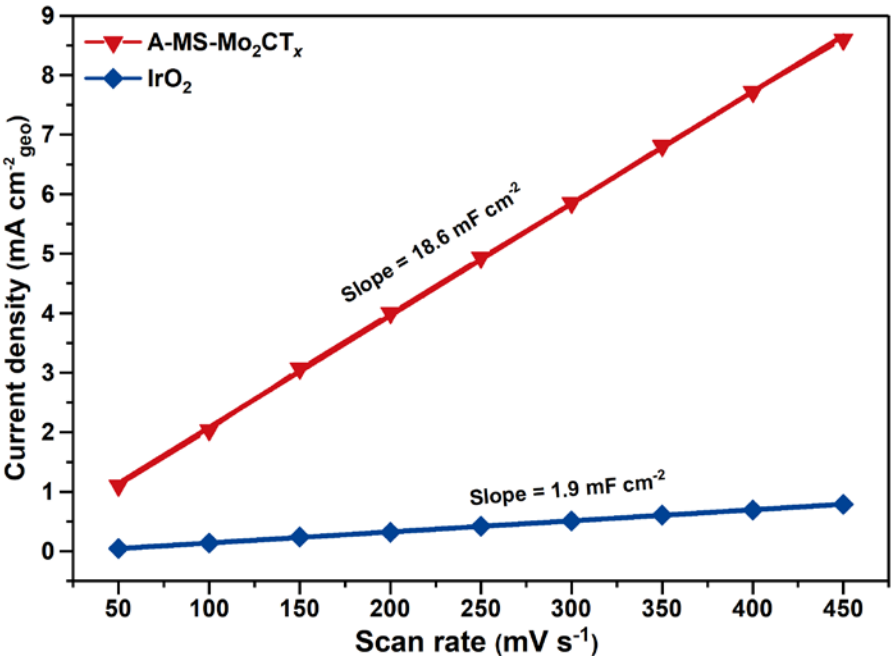

Fig. S30 Double-layer capacitances (C_{dl}) of A-MS-$Mo_2CT_x$and IrO_2.

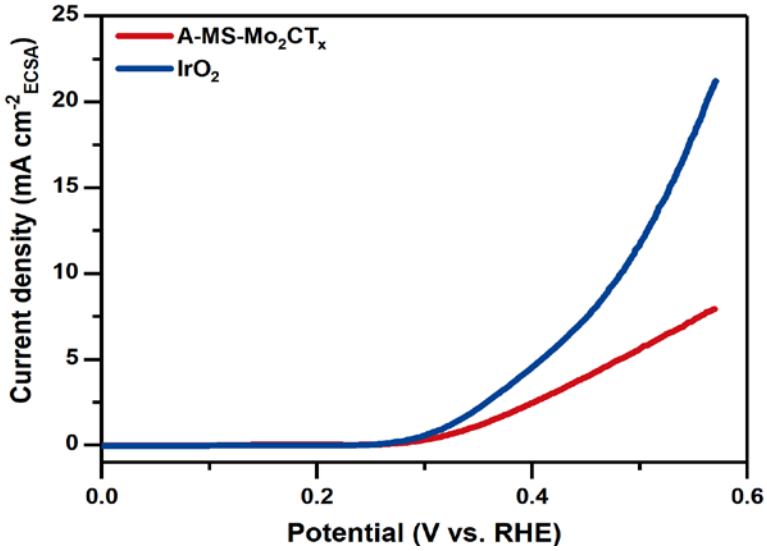

Fig. S31 Electrocatalytic OER specific activity of A-MS-$Mo_2CT_x$and commercial IrO_2 in 1.0 M KOH electrolyte.

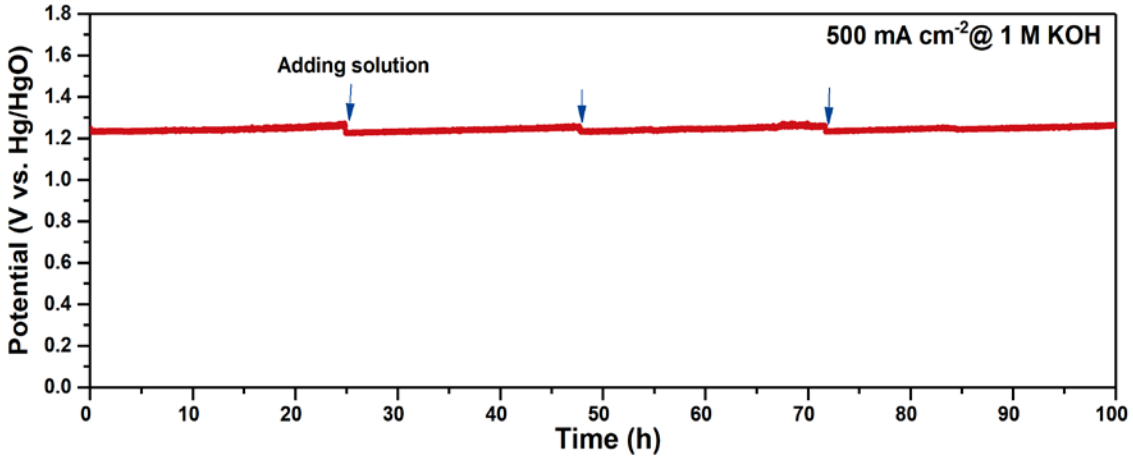

Fig. S32 Long-term stability test of A-MS-Mo_2CT_x in alkaline electrolyte at current density of 500 mA cm^{-2}.

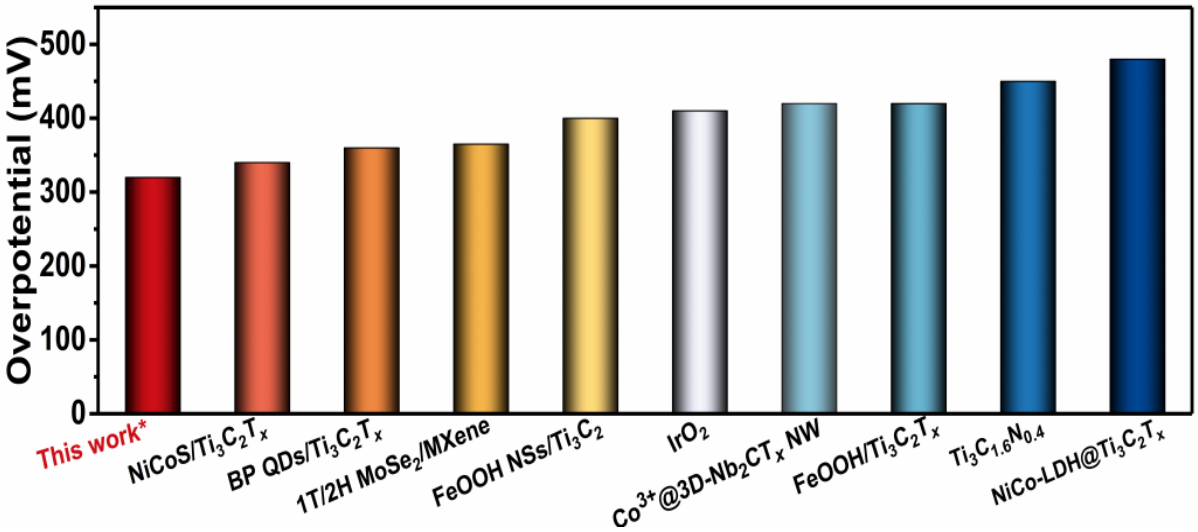

Fig. S33 Overpotentials of reported MXene-based catalystsat the current densityof 10 mA cm^{-2}in 1 M KOH.[5-11]

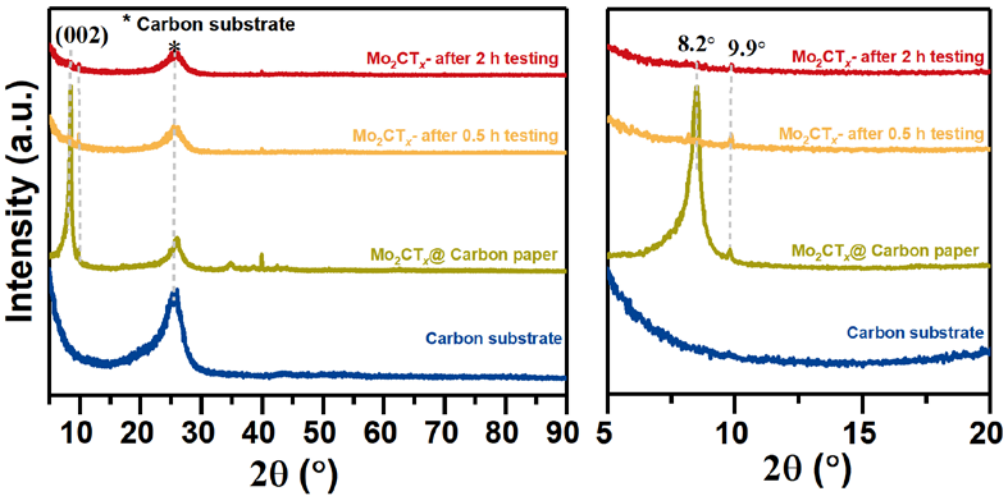

Fig. S34 Ex situ XRD characterization of Mo_2CT_xat 10 mA cm^{-2} current density and different timetesting process. Due to the poor stability of Mo_2CT_x, the testing time is limited to 2h.

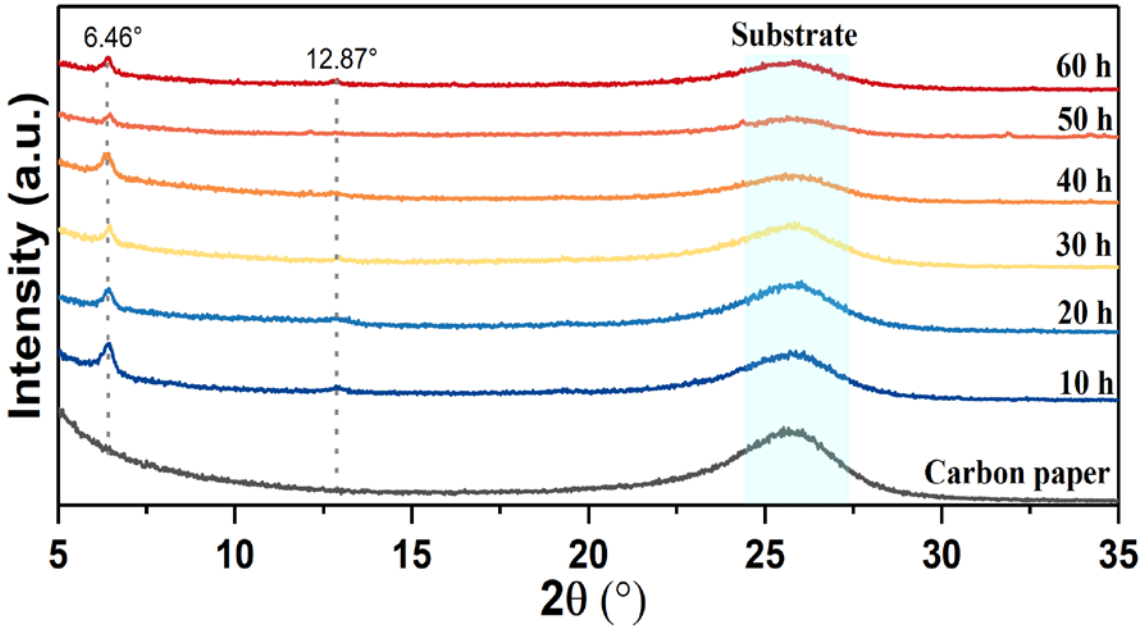

Fig. S35 Ex situ XRD characterization of A-MS-Mo_2CT_xat 10 mA cm^{-2} current density duringdifferent timetesting process.

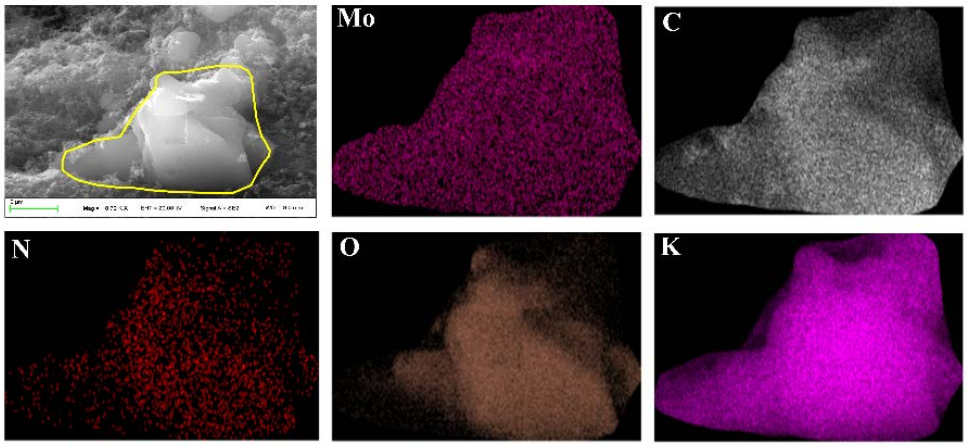

Fig.S36 SEM and EDS of A-MS-Mo_2CT_xafter long-term testing at 500 mA cm^{-2}.

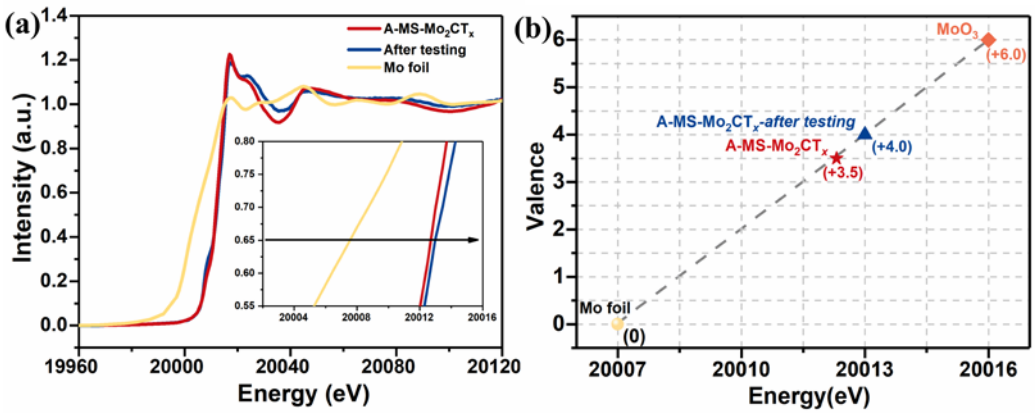

Fig. S37(a) Normalized XANES spectra of A-MS-Mo_2CT_x after long-term testing at current density of 500mA cm^{-2}, (b) the fitted average valence state of Mo.

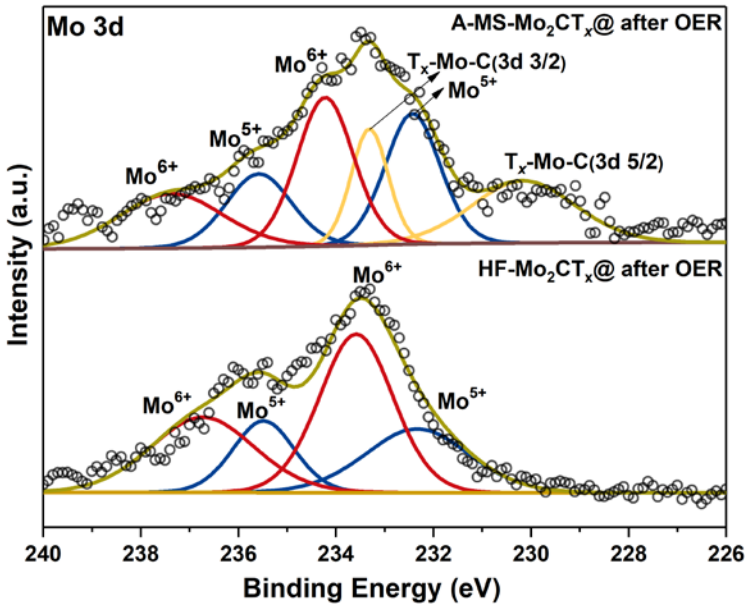

Fig. S38 Mo 3d XPS spectra of A-MS-$Mo_2CT_x$and HF-Mo_2CT_x after OER.

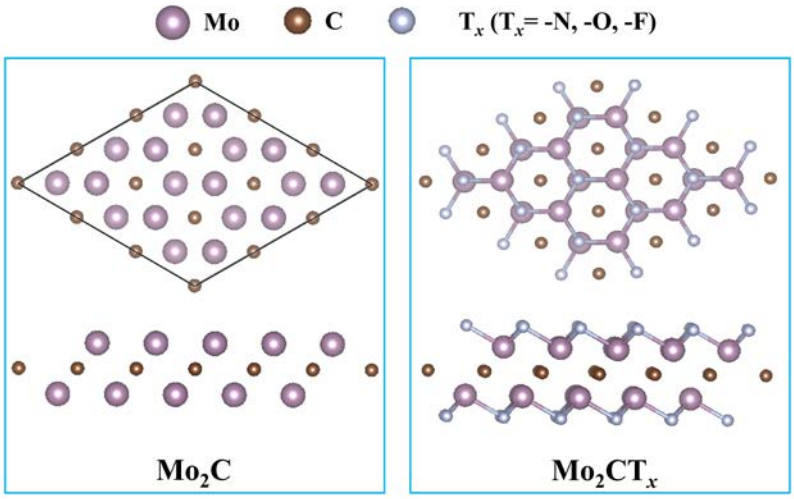

Fig. S39 Model structures of Mo-based surfaces containing different groups.

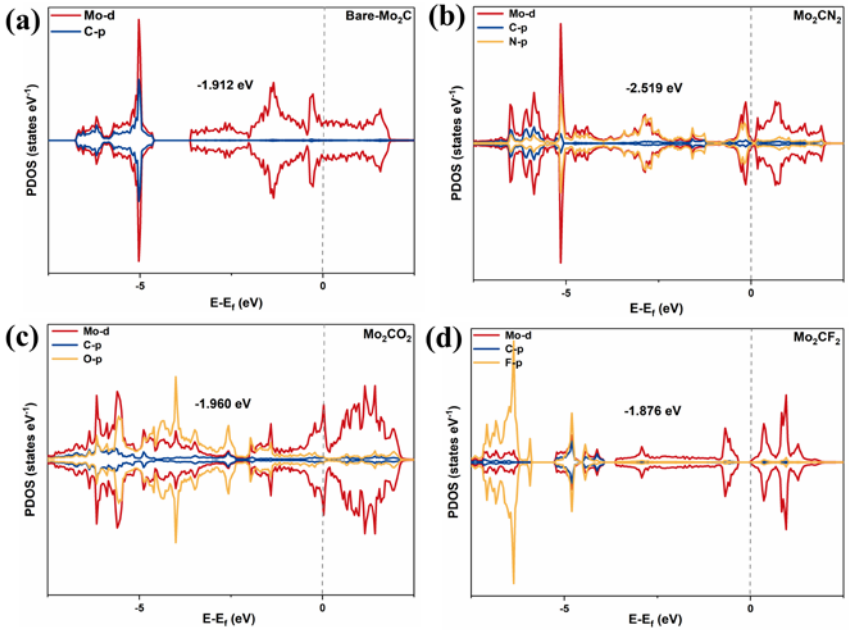

Fig. S40 PDOS and d-band centre of Mo-based MXene without/with different functional groups, (a) Mo_2C, (b) Mo_2CN_2, (c)Mo_2CO_2, (d)Mo_2CF_2.

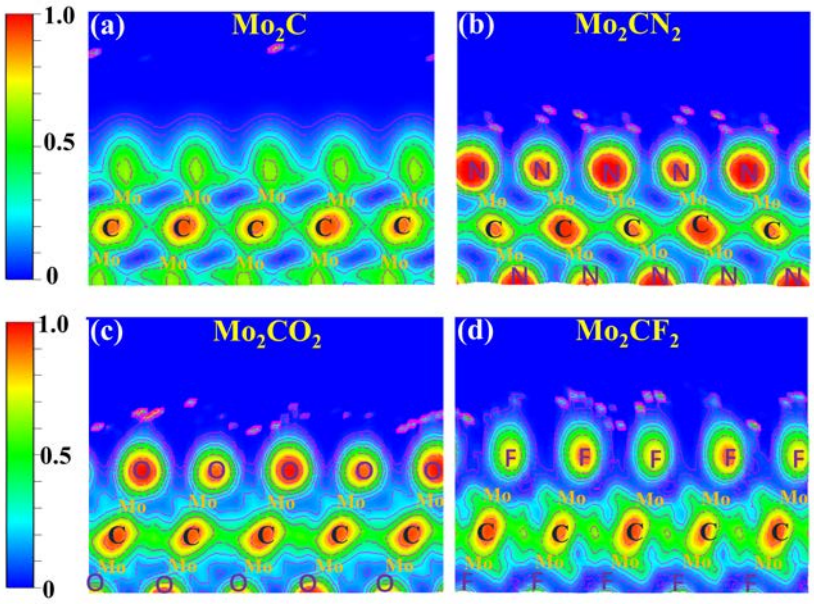

Fig. S41 Electron Localization Function (ELF) of Mo-based MXene without/with different functional groups, (a) Mo_2C, (b) Mo_2CN_2, (c)Mo_2CO_2, (d)Mo_2CF_2.

Table S1. Relativeelement contents (at.%) of A-MS-Mo_2CT_x and Mo_2Ga_2C detected by XPS measurement.

Element concentration (at. %)	Mo (3d)	C (1s)	Ga (2p)	O (1s)	N (1s)
A-MS-Mo_2CT_x	13.30	36.40	1.63	34.71	16.93
Mo_2Ga_2C	13.00	32.90	17.56	36.56	0

Table S2. Deconvolution results of the high-resolution XPS spectrum of the Mo 3d region for Mo_2Ga_2C and A-MS-Mo_2CT_x.

Mo_2Ga_2C	BE (eV)	FWHM (eV)	Fraction(%)	Assigned to
Mo 3d	227.8 (230.9)	0.62 (0.78)	28.23	Mo-C
	228.8 (232.0)	2.00 (2.00)	43.34	Mo^{4+}
	232.2 (235.4)	2.07 (2.00)	28.43	Mo^{5+}
A-MS-Mo_2CT_x	BE (eV)	FWHM (eV)	Fraction(%)	Assigned to
Mo 3d	229.2 (232.4)	1.07 (1.15)	86.95	N-Mo-C
	232.0 (235.1)	1.42 (1.50)	13.05	Mo^{5+}

Table S3. Deconvolution results of the high-resolution XPS spectrum of the C 1s region for A-MS-Mo_2CT_x.

Mo_2Ga_2C	BE (eV)	FWHM (eV)	Fraction(%)	Assigned to
C 1s	283.3	1.22	17.45	Mo-C
	284.8	1.28	52.98	C-C
	285.7	2.0	22.19	C-O
	288.7	2.0	7.07	C=O
A-MS-Mo_2CT_x	BE (eV)	FWHM (eV)	Fraction(%)	Assigned to
C 1s	283.5	1.22	19.26	Mo-C
	284.8	1.33	56.76	C-C
	286.5	1.67	20.29	C-N
	289.0	1.33	3.07	C=O

Table S4. Deconvolution results of the high-resolution XPS spectrum of the N 1s region for A-MS-Mo_2CT_x.

A-MS-Mo_2CT_x	BE(eV)	FWHM (eV)	Fraction (%)	Assigned to
N 1s	395.4	2.58	58.34	Mo 2p
	397.2	0.98	20.46	Mo-N
	398.0	1.07	13.28	Pyridinic N
	399.2	0.93	4.26	Pyrrolic N
	400.3	1.2	3.66	Graphitic N

Table S5. Corresponding fit parameters for Mo foil, A-MS-Mo_2CT_x and Mo_2Ga_2C.

Sample	bond type	CN*	R (Å)	$\sigma^2(10^{-3}Å^2)$**	R factor
Mo foil	Mo-Mo1	8	2.72±0.01	3.3±0.5	0.002
	Mo-Mo2	6	3.15±0.01	3.1±0.7	
A-MS-Mo_2CT_x	Mo-N/C	5.9±0.7	2.11±0.01	4.7±1.4	0.012
	Mo-Mo1	1.9±0.8	2.79±0.02	3.9±2.0	
	Mo-Mo2	5.0±1.3	3.10±0.01	4.6±1.2	
Mo_2Ga_2C	Mo-C	3.0±0.2	2.08±0.01	4.2±1.9	0.004
	Mo-Ga	3.6±0.4	2.73±0.01	4.2±0.7	
	Mo-Mo	4.9±0.5	3.01±0.01	2.9±0.5	

* CN: coordination number; S_0^2 was fixed to be 0.91 from Mo-foil.

** σ^2: Debye−Waller factors.

Table S6. Fitted impendence parameters of A-MS-Mo_2CT_x, IrO_2 and HF-Mo_2CT_x, respectively.

Samples	Series resistance R_s (Ω)	Charge-transfer resistance $R1_{ct}$ (Ω)	Charge-transfer resistance $R2_{ct}$ (Ω)
A-MS-Mo_2CT_x	5.89	-	8.6
IrO_2	6.52	-	58.2
HF-Mo_2CT_x	4.79	11.2	101

Table S7 Deconvolution results of the high-resolution XPS spectrum of the Mo3d region before and after OER

A-MS-Mo_2CT_xafter OER	BE (eV)	FWHM (eV)	Fraction(%)	Assigned to
Mo 3d	230.16 (233.31)	2.50 (0.89)	29.20	T_x-Mo-C
	232.43 (235.58)	1.33 (1.58)	32.60	Mo^{5+}
	234.22 (237.37)	1.37 (2.50)	38.20	Mo^{6+}
HF-Mo_2CT_xafter OER	BE (eV)	FWHM (eV)	Fraction (%)	Assigned to
Mo 3d	232.33(235.481)	2.50 (1.49)	36.17	Mo^{5+}
	233.58 (236.73)	1.78(2.50)	63.83	Mo^{6+}

Table S8. The bond length of different functional group structures

Type	bond	bond length (Å)
Mo_2C	Mo-C	2.20
Mo_2CN_2	Mo-N	2.05
Mo_2CO_2	Mo-O	2.10
Mo_2CF_2	Mo-F	2.30

References

1.E. B. Deeva, A. Kurlov, P. M. Abdala, D. Lebedev, S. M. Kim, C. P. Gordon, A. Tsoukalou,A. Fedorov and C. R. Müller, *Chem. Mater.*, 2019, **31**, 4505-4513.

2.C. Wang, H. Shou, S. Chen, S. Wei, Y. Lin, P. Zhang, Z. Liu, K. Zhu, X. Guo and X. Wu, *Adv. Mater.*, 2021, **33**, 2101015.

3.F. Scharmann, G. Cherkashinin, V. Breternitz, C. Knedlik, G. Hartung, T. Weber and J. Schaefer, Interfaces and thin films, 2004, **36**, 981-985.

4.L.-S. Hsu, *Surf. Sci. Spectra*, 2000, **7**, 122-133.

5.H. Zou, B. He, P. Kuang, J. Yu and K. Fan, *ACS Appl.Mater.*, 2018, **10**, 22311-22319.

6.X.-D. Zhu, Y. Xie and Y.-T. Liu, *J.Mater.Chem. A*, 2018, **6**, 21255-21260.

7.N. Li, Y. Zhang, M. Jia, X. Lv, X. Li, R. Li, X. Ding, Y.-Z. Zheng and X. Tao, *Electrochim. Acta*, 2019, **326**, 134976.

8.K. Zhao, X. Ma, S. Lin, Z. Xu and L. Li, *ChemistrySelect*, 2020, **5**, 1890-1895.

9.S. Y. Pang, W. F. Io, L. W. Wong, J. Zhao and J. Hao, *Adv. Science*, 2020, **7**, 1903680.

10.N. Li, S. Wei, Y. Xu, J. Liu, J. Wu, G. Jia and X. Cui, *Electrochim. Acta*, 2018, **290**, 364-368.

11.Y. Tang, C. Yang, Y. Tian, Y. Luo, X. Yin and W. Que, *Nanoscale Adv.*, 2020, **2**, 1187-1194.